Determining Inner Geometry Properties From Eccentered Pulse-Echo Measurements in a Pipe

Mikael Yuan Estuariwinarno[1], Erlend Magnus Viggen[1],

[1] Centre for Innovative Ultrasound Solutions (CIUS) and Dept. of Circulation and Medical Imaging, Norwegian University of Science and Technology (NTNU), Trondheim, Norway
Contact email: mikael.y.estuariwinarno@ntnu.com

Abstract

In the petroleum industry, well integrity evaluation is an essential part of maintaining the safety and sustainability of hydrocarbon production. Ultrasonic pulse-echo cased hole logging is a widely used type of measurement for well integrity evaluation. It gives insight on casing condition and cement quality through the use of an ultrasonic transducer that ideally rotates around the center of the casing. One of the outputs of this logging is a set of inner geometry properties that describe the position of the tool and the inner radius of the casing. However, inner geometry determination is not straightforward as it has to consider the influence of tool eccentering due to gravity and tool movement, which causes the tool to rotate around another axis than the casing center. Despite its importance and wide implementation, detailed information on inner geometry determination from eccentered measurements has not been published in the scientific literature. In this study, an inner geometry determination algorithm was developed and tested on ultrasonic well log data from from the Norwegian North Sea. This algorithm estimates the inner geometry properties, i.e. the tool eccentering properties and the casing inner radius. The results show that the algorithm produces results that give a good match with the results of a reference algorithm from a service company. Our algorithm is also able to handle poor travel time measurements in a more reliable way than the reference algorithm. Hence, this article attempts to enhance and spread the knowledge of ultrasonic cased hole logging, specifically in terms of the determination of casing inner geometry.

1 Introduction

To produce hydrocarbons, it is necessary to drill a well that attempts to reach a hydrocarbon reservoir in the subsurface. A set of steel pipes, commonly known as casings, are then installed in a newly drilled well. The casings serve several purposes, e.g. preventing the borehole from caving in and providing a conduit from the hydrocarbon reservoir to the surface [1]. Cements are used to bond the casings onto the formation. The presence of cement provides zonal isolation between different zones in the formation and prevents undesirable migration of fluid to the surface through the annulus between the casing and the borehole, commonly known as blowout [2]. Due to their purpose, it is crucial to evaluate the casing condition and cement quality through a well integrity evaluation.

Well integrity is defined as application of technical solutions to maximize the productive life of wells and minimize the risk of uncontrolled release of reservoir fluid over the entire life cycle of the wells [3]. One of the elements in well integrity evaluation is casing

ISBN 978-82-8123-021-7

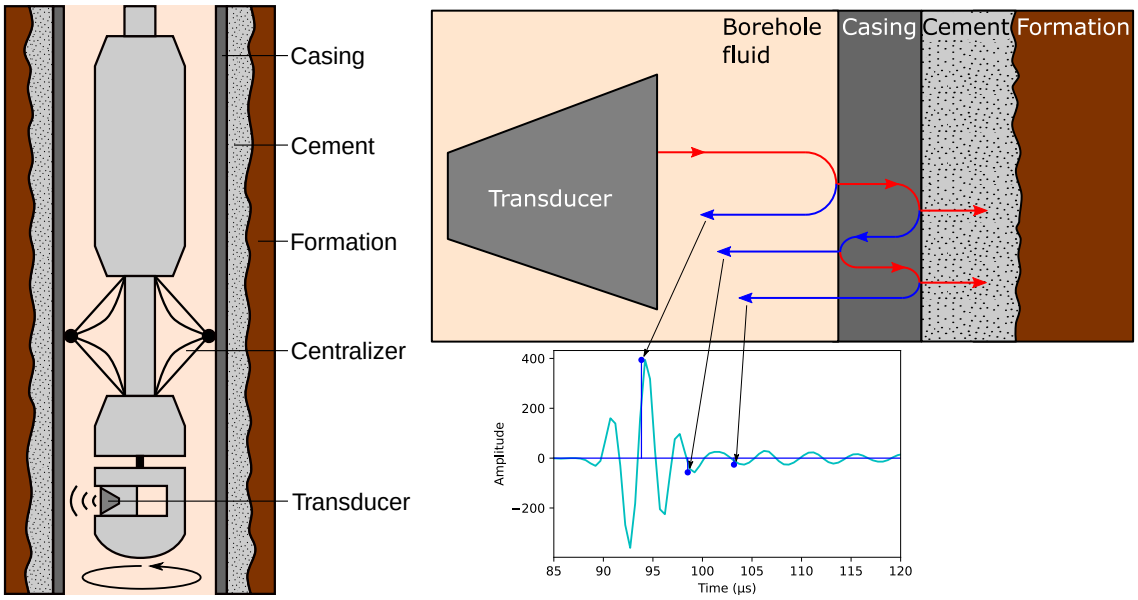

(a) Ultrasonic logging tool (b) Pulse-echo technique

Figure 1: Illustrations of an ultrasonic logging tool and a measurement with pulse-echo technique

and cement evaluation through measurement with an ultrasonic logging tool, also known as ultrasonic cased hole logging. Many ultrasonic logging tools operate based on the pulse-echo technique, in which a rotating transducer fires ultrasonic pulses and records the reflections from the casing and any materials behind the casing (Figure 1b). The tool ideally measures from the center of the casing for every predetermined azimuthal angle of measurement. The recorded waveforms from the reflections are then analyzed to evaluate the casing and cement quality. The outputs of ultrasonic cased hole logging are as follows: [4, 5]

- inner radius of the casing and tool eccentering inside the casing, both based on the measured travel time of the main reflections;
- casing inner rugosity, determined from the amplitude of the main reflection;
- casing thickness, calculated based on the resonant frequency;
- acoustic impedance of the materials behind casing (cement or fluids), based on the shape of the resonance; and
- borehole fluid velocity and impedance, not determined from the same waveform as the previous outputs, but calculated using a different logging mode when the tool is being lowered into the well.

These outputs are all functions of depth and azimuthal angle, with the exception of tool eccentering and borehole fluid properties, which are functions only of depth.

The casing inner radius reflects the casing condition, which may deteriorate over time, e.g. due to corrosion from the subsurface fluid or pressure form the surrounding formation. An ideal casing has an inner geometry with a similar value of inner radius for every azimuthal angle, while a corroded casing might have larger inner radii on some parts of

ISBN 978-82-8123-021-7

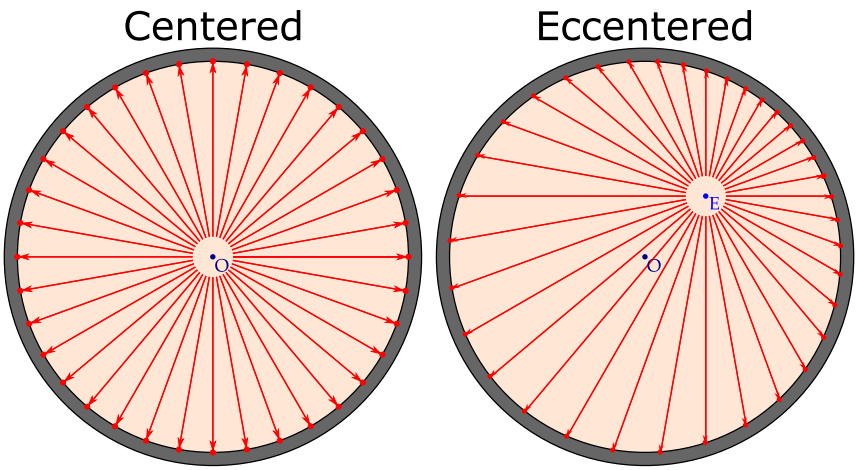

Figure 2: A comparison between centered and eccentered ultrasonic measurements on a cross-section of a well.

the casing due to corrosion. Pressure from the surrounding formation may cause a deformation of the casing shape which leads to a damage. Hence, gaining information about the inner geometry of the casing is important in the evaluation of casing condition.

The estimation of casing inner radius requires an algorithm that takes the eccentering of measurements into account. Such measurements occur when the tool is not rotating around the center of the casing, but from a certain point deviated from the casing center (Figure 2). Eccentering regularly occurs throughout the logging operation due to gravity and tool movement. Since casings generally have a circular geometry, it is desirable to generate inner radius measurements from the center of the casing, to be able to compare them with the reference inner radius. Therefore, the effects of eccentered measurement have to be quantified, and then used to determine the casing inner radius [5].

Although different methods to estimate tool eccentering or inner geometry properties have been documented in several patents [6–8], there is no publicly available scientific article which gives a thorough explanation on inner geometry properties estimation with real case examples. The limited information on a simple yet essential measurement motivated this study, which aimed to develop and publish an algorithm to estimate inner geometry properties of tool eccentering and casing inner radius. This algorithm was developed based on the pulse-echo technique and trigonometric principle, and not from any of the patented methods. Ultrasonic well log data from wells in the Norwegian North Sea were utilized to develop and test the algorithm. What we learned during the development of the algorithm is written in this article to enhance the knowledge of ultrasonic cased hole logging and make it publicly available.

2 Principle of Inner Geometry Calculations

One of the outputs of the pulse-echo technique is the distance from the tool axis to a measurement point on the casing inner perimeter, for every angle of measurement. The tool axis refers to the axis that the tool rotates around. The distance is generated based on the recorded travel time of the ultrasonic pulse which is fired and received by the transducer. The travel time (t_t) refers to the duration from the time when the ultrasonic pulse is fired to the time when the reflection is received by the transducer (cf. Section 3.2). If the tool is

ISBN 978-82-8123-021-7

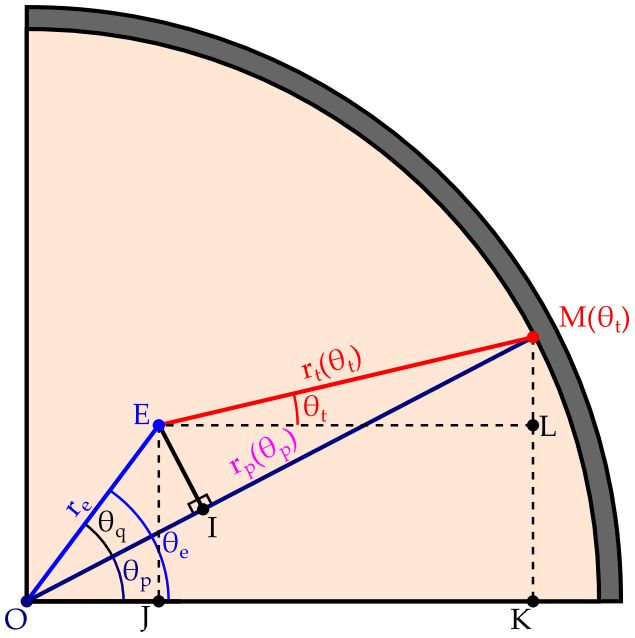

Figure 3: A geometric illustration of an eccentered measurement on a cross-section of a well.

perfectly centered in the casing, this distance, combined with the distance from the tool axis to the transducer, directly give us the inner radius of the casing. However, in an eccentered measurement, this combined distance is not measured from the center of the casing. Hence, the distance cannot be compared directly with the reference casing inner radius to give an insight on the casing condition. The eccentering properties, i.e. eccentering distance and angle, have to be calculated first before we can determine the casing inner radius. To determine the eccentering properties and casing inner radius, a series of trigonometric calculations are performed.

Figure 3 shows a geometric illustration of an eccentered measurement, with the essential geometric notations defined as follows:[1]

- O: The casing center, which is defined as the center of the best-fit circular approximation to the actual shape of the casing (cf. Section 3.3).
- E: The tool axis, which is defined as the axis that the tool rotates around.
- θ_t: The rotation angle of the transducer. It is also referred to as the angle of measurement.
- $M(\theta_t)$: The measurement point on the casing inner perimeter, for a certain angle of measurement θ_t.
- θ_e: The angle from the casing center O to the tool axis E in an eccentered measurement. This angle is also referred to as the eccentering angle.
- θ_p: The angle from the casing center O to the measurement point $M(\theta_t)$. This angle is also referred to as the azimuthal angle.

[1]Many of the quantities defined in this list are functions of both depth z and angle θ. However, as we only need to consider measurements at one depth at a time to find the inner geometry properties, we disregard the depth z in the notation in order to make it less heavy.

ISBN 978-82-8123-021-7

- $r_t(\theta_t)$: The tool-axis-to-casing distance, defined as the line segment $\overline{EM}(\theta_t)$ from the tool axis E to the measurement point $M(\theta_t)$. This distance is calculated based on the recorded travel time $t_t(\theta_t)$ of the ultrasonic pulse. The tool-axis-to-casing distance is the only inner geometry property which is known initially.
- r_e: The eccentering distance, which is defined as the line segment $\overline{OE}$ from the casing center O to the tool axis E.
- $r_p(\theta_p)$: The casing inner radius, which is defined as the line segment $\overline{OM}(\theta_p)$ from the casing center O to the measurement point M on the casing inner perimeter, for a certain azimuthal angle θ_p.

From those definitions, several additional line segments and angles need to be defined in order to determine eccentering properties and casing inner radius. The additional angle and line segments are determined through the following trigonometric equations:

- $\theta_q = \theta_e - \theta_p$: The angle between the measurement point $M(\theta_t)$ and the tool axis E, measured from the casing center O.
- $\overline{OI} = r_e \cos(\theta_q)$: The distance from the casing center O to the point I.
- $\overline{EI} = r_e \sin(\theta_q)$: The distance from the tool axis E to the point I.
- $\overline{IM}$: The distance from the point I to the measurement point $M(\theta_t)$. This line segment is defined as

$$\begin{aligned} \overline{IM} &= \overline{OM} - \overline{OI} \\ &= r_p(\theta_p) - r_e \cos(\theta_q). \end{aligned} \tag{1}$$

  It may also be defined as

$$\begin{aligned} \overline{IM}^2 &= \overline{EM}^2 - \overline{EI}^2 \\ \overline{IM} &= \sqrt{\overline{EM}^2 - \overline{EI}^2} \\ &= \sqrt{r_t^2(\theta_t) - r_e^2 \sin^2(\theta_q)}. \end{aligned} \tag{2}$$

From (1) and (2), we know that

$$r_p(\theta_p) - r_e \cos(\theta_q) = \sqrt{r_t^2(\theta_t) - r_e^2 \sin^2(\theta_q)}. \tag{3}$$

Therefore, the measured tool-axis-to-casing distance $r_t(\theta_t)$ can be expressed as a calculation of other unknown inner geometry properties, e.g. eccentering distance r_e and casing inner radius $r_p(\theta_p)$:

$$\begin{aligned} r_t^2(\theta_t) &= \Big[r_p(\theta_p) - r_e \cos(\theta_q)\Big]^2 + r_e^2 \sin^2(\theta_q) \\ r_t(\theta_t) &= \sqrt{\Big[r_p(\theta_p) - r_e \cos(\theta_q)\Big]^2 + r_e^2 \sin^2(\theta_q)} \\ &= \sqrt{r_p^2(\theta_p) - 2r_p(\theta_p) r_e \cos(\theta_q) + r_e^2 \cos^2(\theta_q) + r_e^2 \sin^2(\theta_q)} \\ &= \sqrt{r_p^2(\theta_p) - 2r_p(\theta_p) r_e \cos(\theta_q) + r_e^2}. \end{aligned} \tag{4}$$

As Figure 4 shows, this relationship is particularly useful when the tool is oriented towards or against the direction of eccentering:

ISBN 978-82-8123-021-7

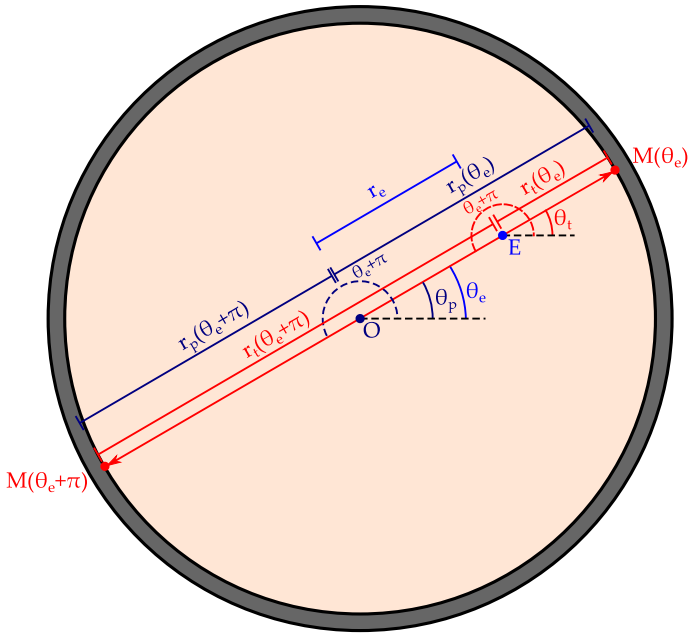

Figure 4: A cross-sectional illustration of a well showing a special case when the eccentered measurement is oriented towards or against the eccentering direction.

- When the tool is oriented towards the eccentering direction, the tool-axis-to-casing distance $r_t(\theta_t)$ is at its shortest. In this case, $\theta_t = \theta_p = \theta_e$, and $\theta_q = \theta_e - \theta_p = 0$. From (4), we have

$$r_t(\theta_e) = \sqrt{r_p^2(\theta_e) - 2r_p(\theta_e)r_e + r_e^2} = \sqrt{\left[r_p(\theta_e) - r_e\right]^2} = r_p(\theta_e) - r_e. \tag{5}$$

- Conversely, when the tool is rotated against the eccentering direction, $r_t(\theta_t)$ is at its longest. In this case, $\theta_t = \theta_p = \theta_e + \pi$, and $\theta_q = \pi$. Equation (4) then becomes

$$r_t(\theta_e + \pi) = \sqrt{r_p^2(\theta_e + \pi) + 2r_p(\theta_e + \pi)r_e + r_e^2} = r_p(\theta_e + \pi) + r_e. \tag{6}$$

If the casing is approximately circular, then $r_p(\theta_e) \approx r_p(\theta_e + \pi)$. Therefore, we can use the maximum and minimum measured $r_t(\theta_t)$ values, and the angles θ_t at which they occur, to estimate the eccentering angle θ_e and the eccentering distance r_e from (5) and (6).

With known values of tool-axis-to-casing distance $r_t(\theta_t)$, eccentering angle θ_e, and eccentering distance r_e, the azimuthal angle can then be calculated as

$$\theta_p = \tan^{-1}\left(\frac{\overline{OK}}{\overline{KM}}\right) = \tan^{-1}\left(\frac{\overline{OJ} + \overline{JK}}{\overline{KL} + \overline{LM}}\right) = \tan^{-1}\left(\frac{r_e\cos(\theta_e) + r_t\cos(\theta_t)}{r_e\sin(\theta_e) + r_t\sin(\theta_t)}\right). \tag{7}$$

Finally, the casing inner radius $r_p(\theta_p)$ can be determined based on (4) as

$$r_p(\theta_p) = \sqrt{r_t^2(\theta_t) - r_e^2\sin^2(\theta_q)} + r_e\cos(\theta_q). \tag{8}$$

3 Inner Geometry Determination Algorithm

The inner geometry determination algorithm estimates the inner geometry properties based on the trigonometric relationship between different distances and angles in the

ISBN 978-82-8123-021-7

pulse-echo measurement. Starting with the known value of travel time, the algorithm calculates the tool-axis-to-casing distance, estimates the eccentering properties, and finally determines the casing inner radius. As shown in Figure 5, the algorithm consists of several steps outlined below:

1. **Travel time evaluation:** Raw travel time measurements $t_t(\theta_t)$ are evaluated in this step. Poor travel time readings (unphysical dropouts) are identified using a median filter and then replaced with empty values, specifically Not a Number values (cf. Section 3.1).

2. **Determination of tool-axis-to-casing distance:** Based on the filtered travel time $t_t(\theta_t)$ and the known borehole fluid velocity c, the tool-axis-to-casing distance $r_t(\theta_t)$ for every depth is calculated (cf. Section 3.2).

3. **Initial estimation of eccentering properties:** The eccentering angle θ_e and distance r_e are initially estimated by evaluating the tool-axis-to-casing distance $r_t(\theta_t)$ values for every angle of measurement θ_t and depth. By implementing quadratic regression to estimate the maximum and minimum $r_t(\theta_t)$, we can obtain the initial estimates of eccentering properties (cf. Section 3.3).

4. **Refined estimation of eccentering properties:** In this step the initial eccentering properties estimates are refined by curve-fitting modelled tool-axis-to-casing distances $r'_t(\theta_t)$ to the previously calculated $r_t(\theta_t)$ values, using a least-squares optimisation method. This results in more accurate estimates of the eccentering properties (cf. Section 3.4).

5. **Determination of casing inner radius:** The final step calculates the casing inner radius $r_p(\theta_p)$ for every depth, based on the calculated tool-axis-to-casing distance $r_t(\theta_t)$ and the refined eccentering properties estimates which are obtained from the previous steps (cf. Section 3.5).

Well log data from wells in the Norwegian North Sea was utilized to develop and test the algorithm in this study. This well log data has the same form as the well integrity logs in the publicly available Volve Data Village dataset [9, 10]. Therefore well log data from this dataset can also be utilized to experiment with this algorithm. The well log shown throughout this article was generated by an ultrasonic logging tool which performs a pulse-echo measurement for every 5° of the transducer's rotation.

3.1 Travel Time Evaluation

The first step in the algorithm is travel time evaluation to remove poor travel time readings, which are referred as unphysical dropouts in this study. Unphysical dropout is defined as a randomly occurring travel time value with a relatively significant difference compared to its neighbors. In the image plot[2] of travel time from each angle of measurement $t_t(\theta_t)$ against depth shown in Figure 6a, unphysical dropouts appear as the randomly occurring pixels with distinct values compared to their neighboring pixels. It is actually possible to have a dropout in the travel time data due to physical damage in

[2] An image plot or image log, which is commonly used to visualize ultrasonic cased hole measurements, is essentially an unwrapped cylinder which represents the casing. This is because the casing and the well itself is approximately cylindrical.

ISBN 978-82-8123-021-7

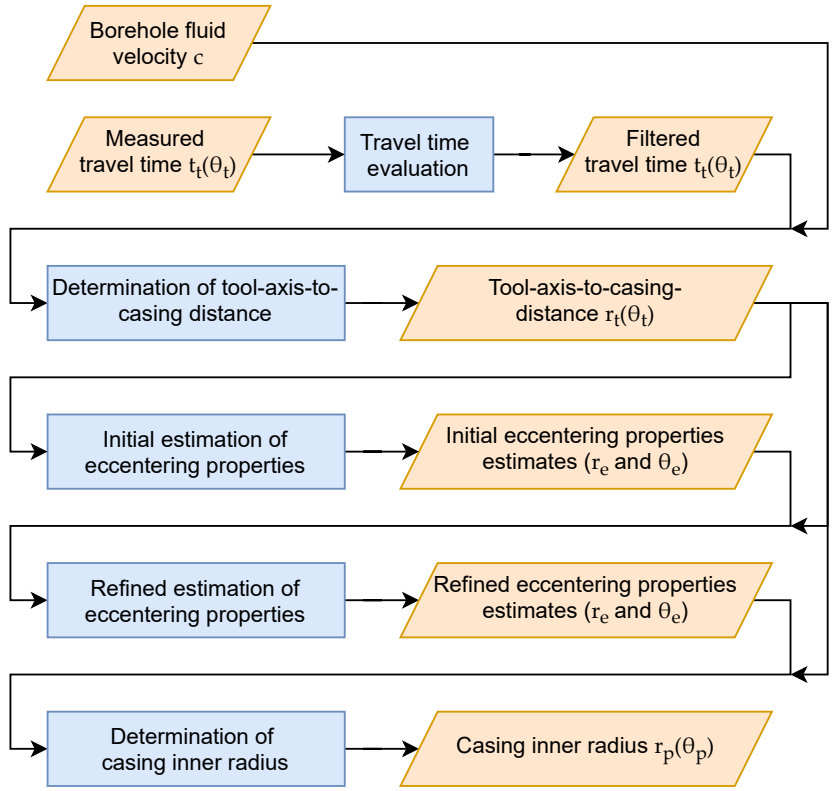

Figure 5: Workflow of the inner geometry determination algorithm. The orange parallelograms represent inputs or outputs, while the blue rectangles represent the steps of the algorithm.

the casing, e.g. hole or crack due to corrosion or deformation of the casing. However, unlike the physical dropout, an unphysical dropout occurs randomly and does not exhibit a gradually increasing or decreasing pattern when compared with its neighbors. A dropout with such characteristics can be considered as unphysical dropout that does not represent the actual condition of the casing.

Through further investigation, it was found that the randomly existing dropouts occur due to the recorded travel time values being outside of the main reflection's envelope when plotted alongside the waveform. Ideally, the recorded travel time of the main reflection should be at the center of the main reflection's envelope. However, when the recorded travel time is significantly higher or lower, the travel time will appear as an unphysical dropout. The dropouts are possibly caused by signal processing errors or electronic failures in the tool. Due to their nature, unphysical dropouts should not be considered as actual measurements, and therefore should be handled properly.

In this step, a median filter is used to evaluate each of the pixels in the raw travel time data from the well log. The median filter used in this step is a horizontal filter with a kernel size of 1×5. This filter evaluates the value in each pixel and then compares it to the median value of itself and the two neighboring pixels on its left and the two on its right side.[3] When the absolute difference between the value and the median exceeds a predetermined threshold, the evaluated pixel is identified as a dropout. In this study, we

[3]On pixels that are situated close to the left and right edge of the travel time array and have less than two neighbors on one side, the filter will use the pixels from the other side of the array as the neighbor. As the travel time array is essentially an unwrapped cylinder representing the casing as in the image plot, pixels on the sides of the array are actually neighbors.

ISBN 978-82-8123-021-7

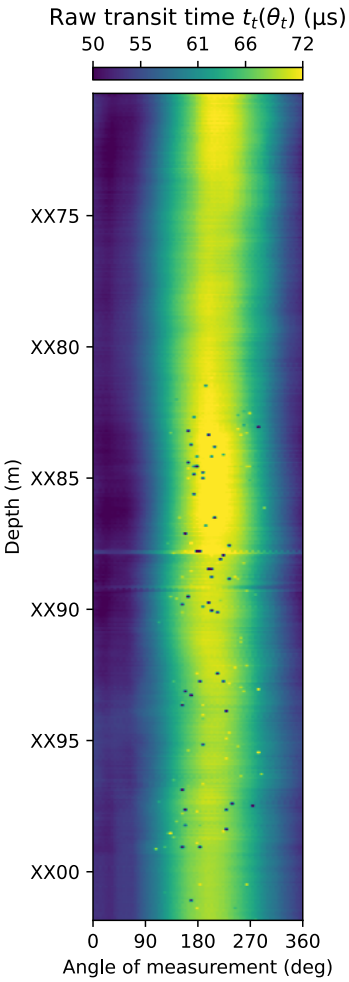

(a) Plot of raw travel time from each angle of measurement.

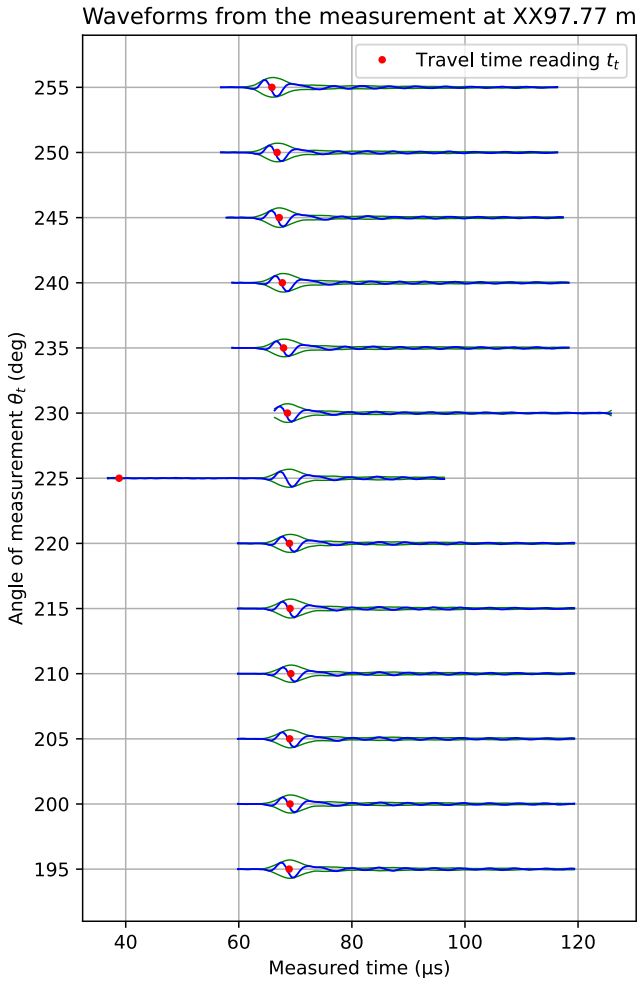

(b) Selected waveforms from the pulse-echo measurement for a certain depth.

Figure 6: A travel time plot to the right shows unphysical dropouts as randomly occurring and distinctly colored pixels. After further investigation, it was found that the dropouts occur due to poor travel time readings as seen to the right at $\theta_t = 225°$.

used a threshold value of 2.5 µs which we found to be appropriate for our data.

It is actually possible to replace an identified dropout with a more sensible value, e.g. the median value from the neighboring pixels or a value from interpolation. However, an artifical value like this does not necessarily provide an actual representation of the casing condition. Therefore in this algorithm, the identified dropout is replaced by an empty value, i.e. a Not a Number (NaN) value. Figure 7 shows how the travel time evaluation generates filtered travel time data with several empty pixels that correspond to unphysical dropouts. The other steps of the algorithm will ignore the NaN values and only use the valid travel time values in the estimation of inner geometry properties. Therefore, the inner geometry properties, e.g. tool-axis-to-casing distance and casing inner radius, will also be represented with NaN values in measurement points with unphysical dropout.

3.2 Determination of Tool-Axis-to-Casing Distance

In the second step of the algorithm, the distances from the tool axis to casing are determined using the filtered travel time $t_t(\theta_t)$ value from the previous step. With a known

ISBN 978-82-8123-021-7

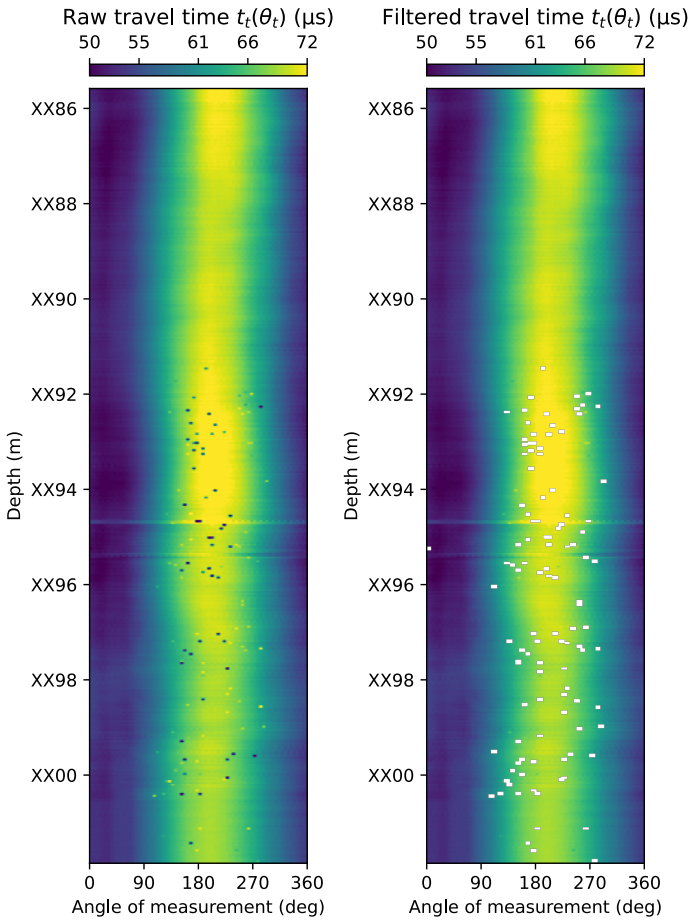

Figure 7: A comparison of travel time data before and after travel time evaluation. The white pixels in the filtered travel time plot corresponds to unphysical dropout values that have been replaced with NaN values.

borehole fluid velocity[4] c and the transducer outer radius r_{tr} from the well log data, the tool-axis-to-casing distance $r_t(\theta_t)$ can be calculated as

$$r_t(\theta_t) = \frac{t_t(\theta_t)}{2}c + r_{tr}. \tag{9}$$

Here, the transducer outer radius r_{tr} is introduced to the calculation because the transducer is measuring from a certain distance from the tool axis (Figure 8). The calculation of tool-axis-to-casing distance is performed for each angle of measurement at every depth.

3.3 Initial Estimation of Eccentering Properties

As discussed in Section 1, eccentered measurements frequently occur due to gravity and tool movement. To compensate for this, we first need to estimate the eccentering distance r_e and angle θ_e, which are required in the trigonometric calculations for the casing inner radius. When estimating these eccentering properties, defining the casing center is essential, as it represents a reference for the eccentered tool. In this algorithm, the casing

[4]The borehole fluid velocity value from the tool's output can be used to calculate $r_t(\theta_t)$ here. This value can also be specified by the operator company. For the well log shown in this article, we used the value from the operator.

ISBN 978-82-8123-021-7

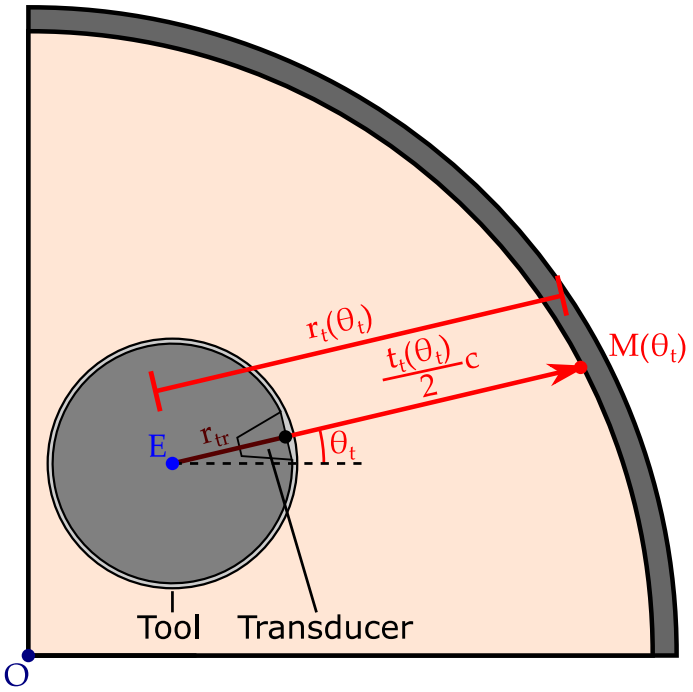

Figure 8: An illustration showing the transducer's position with respect to the tool axis on a section of a well.

center is defined as the center of a circle that gives a best fit to the casing, which is nearly circular.

The initial estimation of eccentering properties is performed based on the values of tool-axis-to-casing distance $r_t(\theta_t)$ over angle of measurement θ_t, for every depth. As explained in Section 2, $r_t(\theta_t)$ is minimal and maximal when it points towards ($\theta_t = \theta_e$) and against ($\theta_t = \theta_e + \pi$) the direction of eccentering, respectively. As seen in Figure 9, by analyzing the $r_t(\theta_t)$ values at each depth, we can find the maximum and minimum value of $r_t(\theta_t)$ and the angles θ_{tmax} and θ_{tmin} at which they occur. Ideally, θ_{tmax} and θ_{tmin} should differ by 180°. Therefore, the eccentering angle θ_e can ideally be estimated from either θ_{tmax} or θ_{tmin}, i.e. $\theta_e \approx \theta_{tmin}$ or $\theta_e + \pi \approx \theta_{tmax}$. However, in most of the cases, θ_{tmax} and θ_{tmin} do not necessarily differ by 180°. Because θ_{tmin} is approximately equal with $\theta_{tmax} + \pi$, the eccentering angle θ_e can be estimated as the mean of θ_{tmin} and $\theta_{tmax} + \pi$. The mean of angles equation is used to estimate the eccentering angle:

$$\theta_e = \tan^{-1}\left(\frac{\sin(\theta_{tmin}) + \sin(\theta_{tmax} + \pi)}{\cos(\theta_{tmin}) + \cos(\theta_{tmax} + \pi)}\right). \tag{10}$$

The eccentering distance r_e is estimated based on the maximum and minimum $r_t(\theta_t)$ using (5) and (6). If the casing is approximately circular, then $r_p(\theta_e) \approx r_p(\theta_e + \pi)$, i.e. $r_p(\theta_{tmin}) \approx r_p(\theta_{tmax})$, and r_e can be estimated as

$$r_e = \frac{r_t(\theta_{tmax}) - r_t(\theta_{tmin})}{2} \tag{11}$$

In this algorithm, the process of finding the maximum and minimum $r_t(\theta_t)$ for every depth is performed by investigating multiple points around the peak and trough of the $r_t(\theta_t)$ curve. Using quadratic regression on those points, we maximum and minimum value are estimated. However, this process has several limitations:

ISBN 978-82-8123-021-7

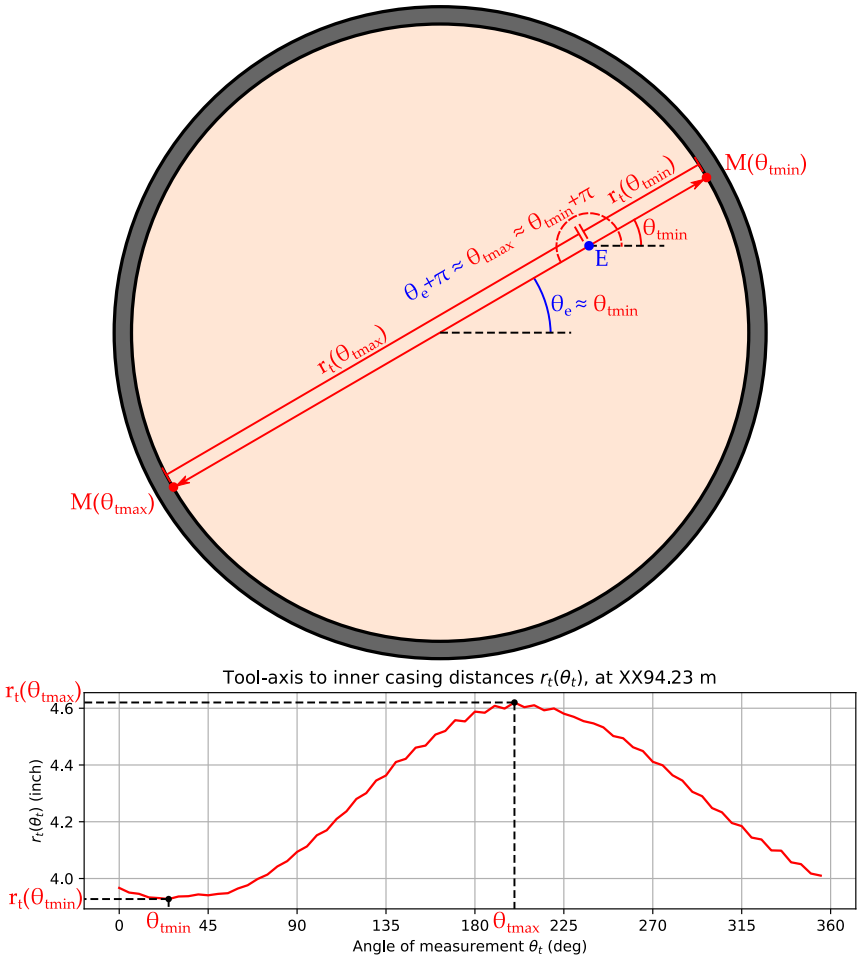

Figure 9: A cross-sectional illustration of a well showing maximum and minimum $r_t(\theta_t)$ value and the angle at which they occur, θ_{tmax} and θ_{tmin}, respectively. The eccentering angle θ_e can be estimated from θ_{tmin}.

- Determining the actual peak and trough can be difficult if the curve is jagged, which may actually reflect the rugosity of the casing inner wall. This implies that the accuracy of the estimated maximum and minimum $r_t(\theta_t)$ value from the quadratic regression is hindered by the jaggedness of the curve.
- The maximum and minimum $r_t(\theta_t)$ value might not necessarily differ by 180°, which induces a significant uncertainty in the eccentering angle.
- The process only considers the peak and the trough of $r_t(\theta_t)$, and does not take the full curve into account.

These limitations motivate the algorithm's next step of refining the estimation of the eccentering properties.

3.4 Refined Estimation of Eccentering Properties

This step refines the initial estimate of the eccentering properties from the previous step. Instead of using a simple quadratic regression on the peak and trough of $r_t(\theta_t)$, the refinement introduces curve-fitting using a least-squares optimization method. By finding

ISBN 978-82-8123-021-7

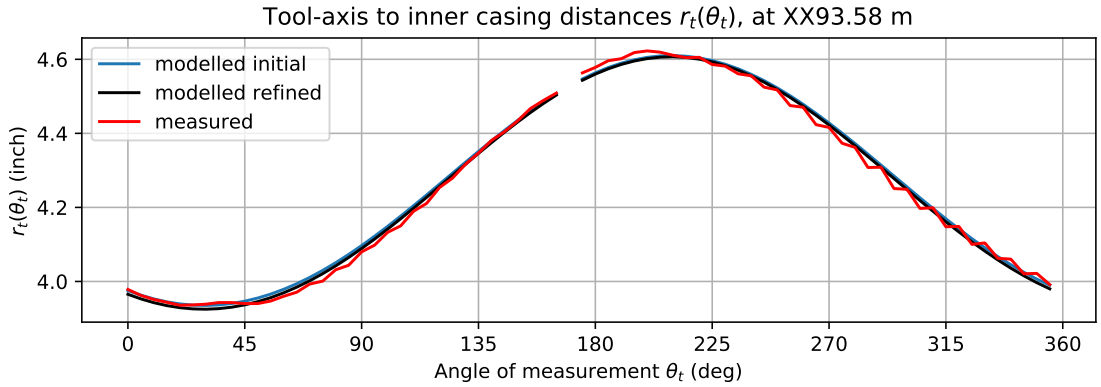

Figure 10: A plot of tool-axis-to-casing distances showing how the refined eccentering properties generated a modelled $r_t(\theta_t)$ curve with a better fit to the measured $r_t(\theta_t)$ than the curve generated by the initial eccentering properties from Section 3.3. Note that the gap around 170° represents the NaN value due to an unphysical dropout.

the best-fit between a modelled tool-axis-to-casing distance $r'_t(\theta_t)$ from this step and the measured $r_t(\theta_t)$ from the second step of the algorithm (cf. Section 3.2), we can find the eccentering properties more accurately.

The modelled $r_t(\theta_t)$ values are calculated based on Equation (4) with a modelled casing inner radius r'_p instead of the regular casing inner radius $r_p(\theta_p)$:

$$r'_t(\theta_t) = \sqrt{r'^2_p - 2r'_p r_e \cos(\theta_e - \theta_p) + r_e^2}. \tag{12}$$

Here, r'_p, r_e and θ_e are free parameters to be optimized using a least-squares optimization method to generate a better-fitting $r'_t(\theta_t)$ curve to the measured $r_t(\theta_t)$. The optimization algorithm requires initial values of these parameters. The initial eccentering distances and angles from the third step of the algorithm (cf. Section 3.3) are used as the initial value of r_e and θ_e. The initial values of r'_p can be calculated from (5) and (6). Assuming that the casing is approximately circular, then $r_p(\theta_e) \approx r_p(\theta_e + \pi)$, i.e. $r_p(\theta_{tmin}) \approx r_p(\theta_{tmax})$, and r'_p can be calculated as

$$r'_p = \frac{r_t(\theta_{tmax}) + r_t(\theta_{tmin})}{2}. \tag{13}$$

In an eccentered measurement, the azimuthal angles θ_p are not evenly sampled as in the angle of measurement θ_t (Figure 2). This implies that the 5° sampling in θ_t does not lead to a 5° sampling in θ_p. Therefore, the unknown parameter θ_p in (12) has to be calculated first using (7) as

$$\theta_p = \tan^{-1}\left(\frac{r_e \cos(\theta_e) + r_t \cos(\theta_t)}{r_e \sin(\theta_e) + r_t \sin(\theta_t)}\right). \tag{14}$$

The least-squares optimization method is implemented to find a more accurate estimate of r_e and θ_e which gives the optimal fit between the modelled $r'_t(\theta_t)$ and measured $r_t(\theta_t)$ at every depth. Figure 10 shows the how the eccentering properties from least-squares optimisation method generated a better-fitting curve than the curve generated by initial eccentering properties from Section 3.3.

ISBN 978-82-8123-021-7

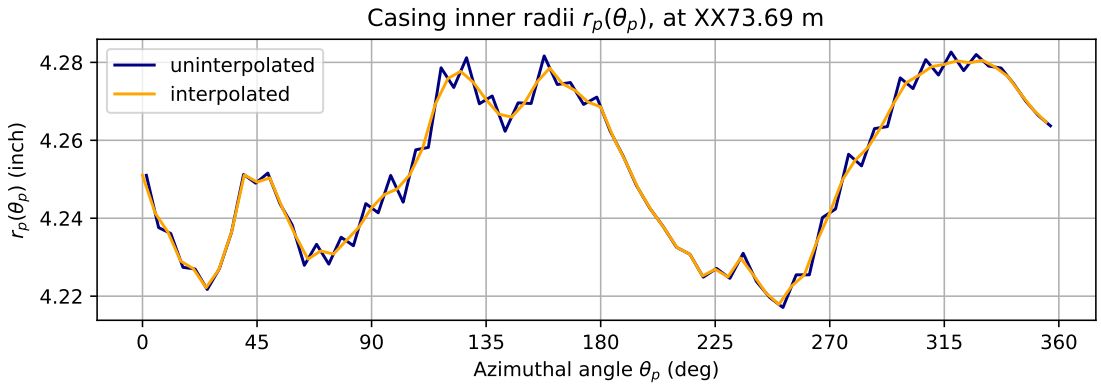

Figure 11: A plot of casing inner radii showing the interpolated inner radius curve smooths away some jagged part of the original curve. This might give a false impression of the rugosity of the casing inner surface.

3.5 Determination of Casing Inner Radius

The final step of the algorithm estimates the casing inner radius $r_p(\theta_p)$ based on the calculated tool-axis-to-casing distance $r_t(\theta_t)$ and eccentering properties r_e and θ_e from the previous steps. Using Equation (14), the azimuthal angle θ_p must be calculated first with the refined values of the eccentering properties from the previous step. The inner radius is calculated using (8) which can be written as

$$r_p(\theta_p) = \sqrt{r_t^2(\theta_t) - r_e^2 \sin^2(\theta_e - \theta_p)} + r_e \cos(\theta_e - \theta_p). \tag{15}$$

Since the azimuthal angles θ_p are estimated from based on the other inner geometry properties, the resulting θ_p are not evenly sampled, unlike the angles of measurement θ_t. We have the option to resample θ_p evenly through interpolation, as Figure 11 shows. However, we can see that this interpolation smooths away jaggedness in some parts of the original $r_p(\theta_p)$ curve. The jaggedness in the $r_p(\theta_p)$ curve might indicate the actual rugosity of casing inner surface. Therefore, smoothing away the jaggedness might give a false impression that the inner surface appears smoother than it actually is.

The downside of using the uninterpolated $r_p(\theta_p)$ values is that the measurement points are not distributed evenly, i.e. they are more tightly packed on one side of the casing compared to the opposite side (Figure 12). In the example shown in Figure 12, for a set of eccentered measurements with an angle of measurement $\theta_t = 10^\circ$, the interpolated $r_p(\theta_p)$ is sampled evenly every 10° as well. On the other hand, the uninterpolated $r_p(\theta_p)$ from the same set of measurements are sampled unevenly. Hence, the the uninterpolated inner radius image plot will have some stretched and squeezed portions due to uneven sampling of θ_p, especially when the eccentering distance r_e is large.

If the eccentering distance is large, the measurement points are even more unevenly distributed. However, since the eccentering distance does not vary significantly from depth to depth, the impact of uneven θ_p sampling in the inner radius image plot is not significant. We also have to note that the measurement points for the interpolated $r_p(\theta_p)$ are artificial, while in the uninterpolated $r_p(\theta_p)$ they are the actual measurement points from eccentered measurements. Therefore in this algorithm, we decided to keep the uninterpolated $r_p(\theta_p)$ values.

ISBN 978-82-8123-021-7

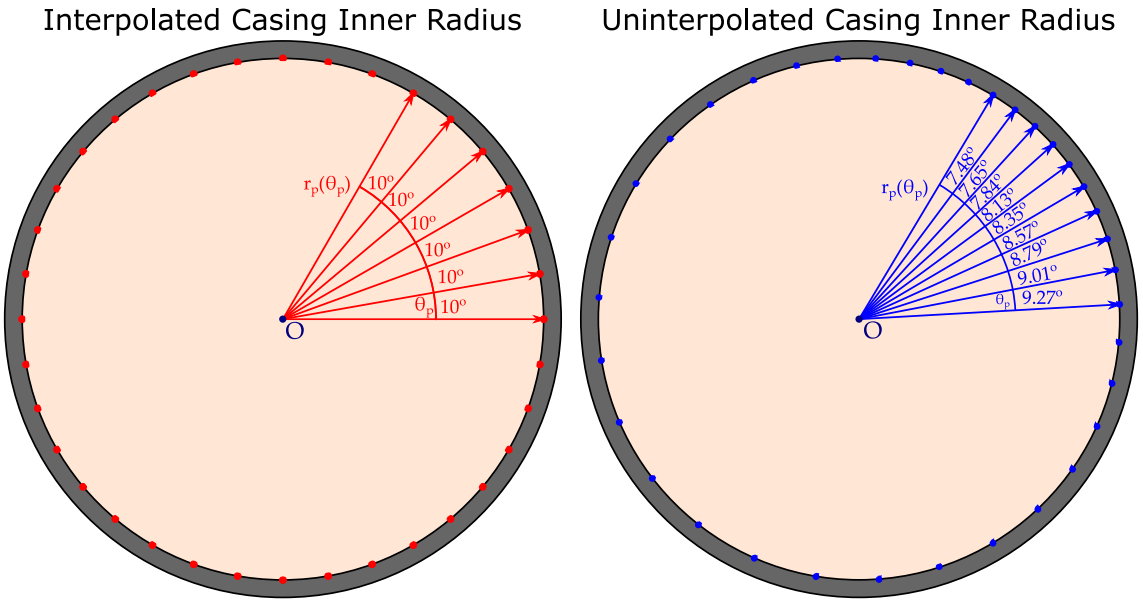

Figure 12: A cross-sectional illustration of a well showing the difference between interpolated and uninterpolated $r_p(\theta_p)$ from the same set of eccentered measurements. The dots on the inner perimeter corresponds to the measurement points. The tool axis position in the eccentered measurement is shown in Figure 2.

4 Comparison of Results With the Reference Algorithm

The well log data used in this study contains inner geometry data generated by an algorithm from the service company that logged the well. In this study, we refer to the algorithm from the service company as the reference algorithm. The results from our algorithm were compared with the results of this reference algorithm to investigate whether the two come up with the same values for the casing inner geometry properties.

One of the differences between our algorithm and the reference is the way it handles unphysical dropouts at the beginning of the algorithm. In the algorithm developed in this study, the unphysical dropouts are identified using a median filter and filtered out by replacing them with NaN values (cf. Section 3.1) which are ignored in later steps of the algorithm. Hence, instead of using the raw travel time data, the rest of our algorithm utilizes the filtered travel time data as its basis. The effect of the different dropout handling can be seen in the the results in this section.

4.1 Comparison of Eccentering Properties

The first inner geometry properties to be estimated are the eccentering properties. Our algorithm estimates two different sets of eccentering properties, namely the initial and refined eccentering properties. These can be compared with the eccentering properties from the reference algorithm. Figure 13 compares the initial eccentering properties estimated by our algorithm and the eccentering properties from the reference algorithm. The figure shows a quite good match in the eccentering properties between our initial estimate and the reference algorithm. The trend of the initial eccentering distance and angle curves matches the reference curves. For the initial eccentering magnitude, the median of absolute deviation is 0.0027 in, and the median of relative deviation is 0.99%. For

ISBN 978-82-8123-021-7

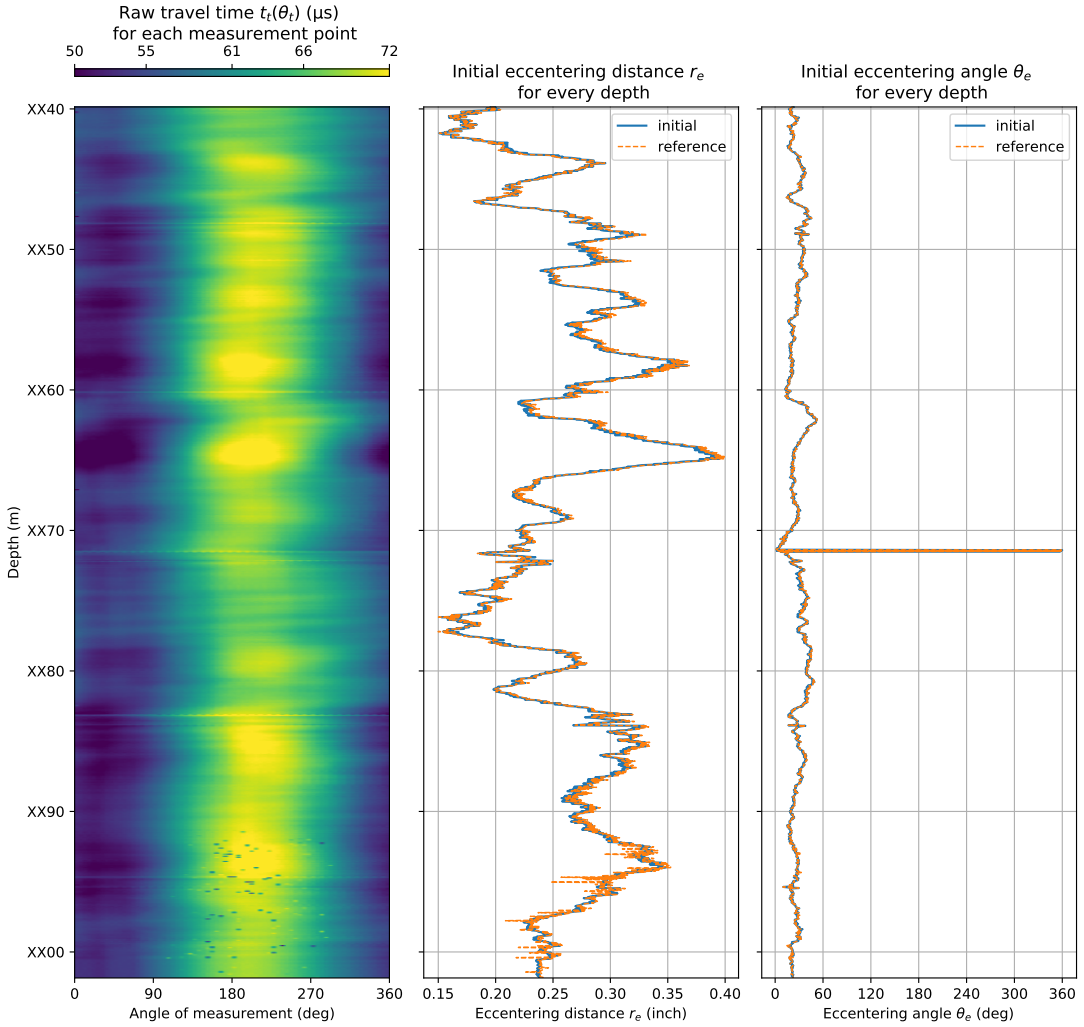

Figure 13: A comparison between the initial eccentering properties estimated by our algorithm and the properties from the reference algorithm, shown in the plots in the center and on right. These properties are correlated with the variation in travel time shown in the image plot on the left.

the initial eccentering angle, the median of absolute deviation is 0.363°, and the median of relative deviation is 1.35%.

The eccentering properties are estimated based on tool-axis-to-casing distance $r_t(\theta_t)$. This implies that these properties are correlated to the travel time, because $r_t(\theta_t)$ is calculated based on the travel time measurement. From Figure 13 we can see that the change in the maximum and minimum value of the travel time is correlated with the change in the eccentering distance curve, and that the change in the maximum and minimum angle of the travel time is correlated with the change in the eccentering angle curve.

Figure 13 also shows the effect of unphysical dropouts on the eccentering distance. We can see multiple leftward spikes on the reference eccentering distance curve, in the interval between XX92 m and XX01 m. These spikes are present in the reference curve, but not in our eccentering distance curve. This is due to the different way of handling dropouts between our algorithm and the reference algorithm. The reference algorithm does not seem to rectify these dropouts, so that the raw travel time data, including some unrealistic values, were used as the basis for the estimation of the inner geometry prop-

ISBN 978-82-8123-021-7

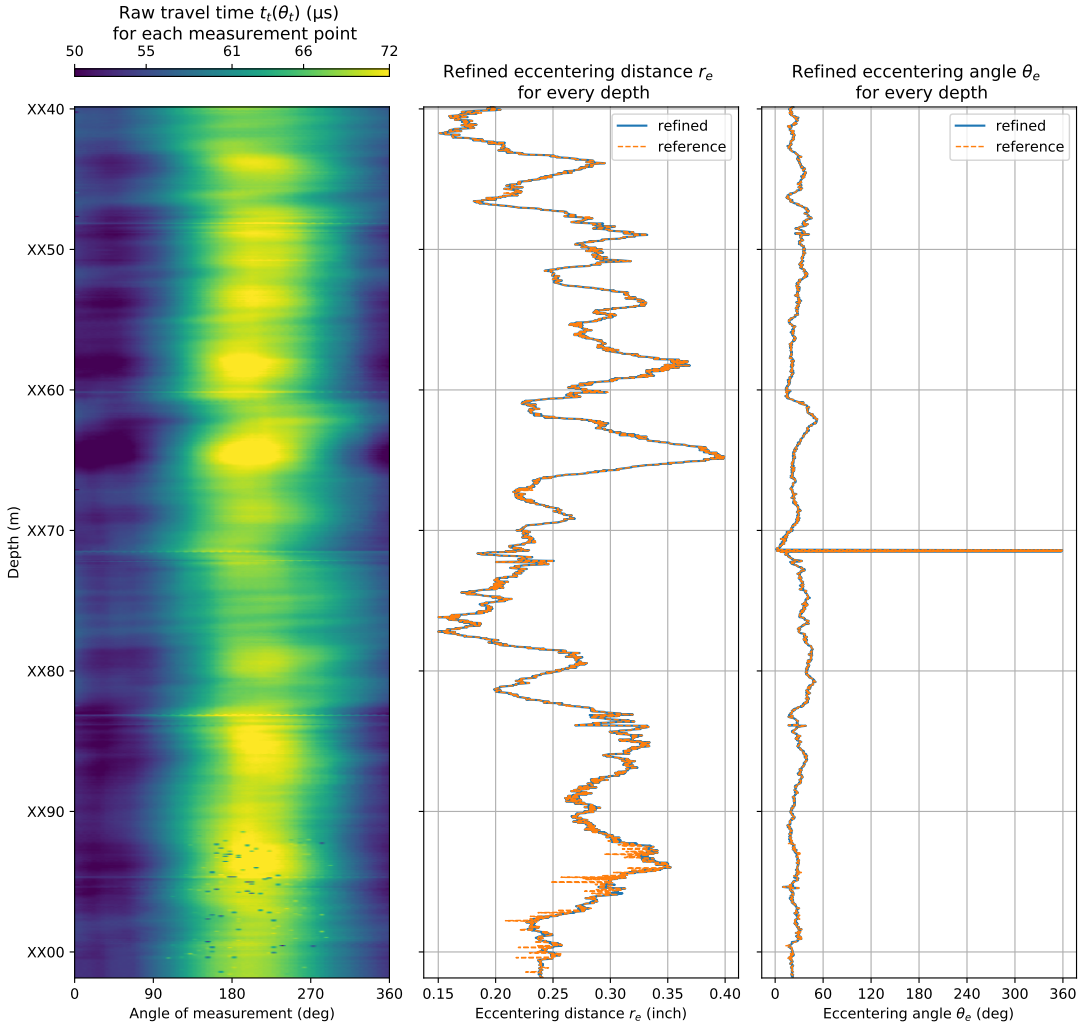

Figure 14: A comparison between the refined eccentering properties estimated by our algorithm and the properties from the reference algorithm, plotted as in Figure 13.

erties. For some particular depths with multiple dropouts, the effect of the unrealistic travel time values on the eccentering distance are amplified, resulting in those spikes. In our algorithm, the dropouts are replaced with NaN values which are ignored in the inner geometry property estimation. Thus, the spikes are not present in our initial eccentering distance curve. Thus, our way of handling dropouts is not only an attempt to generate more reliable data, but it also represents an improvement to the reference algorithm.

Our algorithm's refined estimation of eccentering properties are even closer to the reference, as Figure 14 shows. In some intervals where the initial eccentering properties in Figure 13 are generally slightly smaller than the reference, e.g. XX50 to XX65 m and XX85 to XX90 m, the refined eccentering properties show a better match with the reference. This is also indicated in the deviation values, which are significantly minimized with the refined estimation. For the refined eccentering magnitude, the median of absolute deviation is 4.94×10^{-6} in, and the median of relative deviation is 0.0019%. For the refined eccentering angle, the median of absolute deviation is 0.0015°, and the median of relative deviation is 0.0058%.

ISBN 978-82-8123-021-7

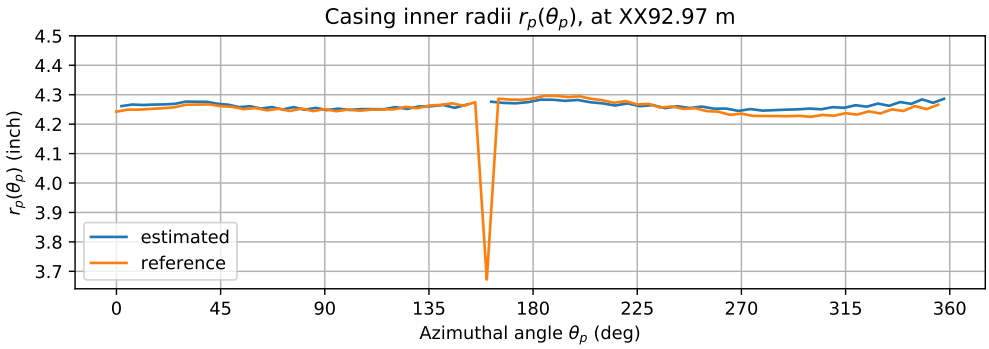

Figure 15: A comparison between the inner radius $r_p(\theta_p)$ from our algorithm and from the reference algorithm at one depth. Note that the impact of an unphysical dropout at the measurement around 170° is represented by a gap on the estimated curve, and a downward spike on the reference curve.

4.2 Comparison of Casing Inner Radius

The second inner geometry property estimated by both algorithms is the casing inner radius $r_p(\theta_p)$. Figure 15 shows a comparison between the casing inner radius estimated by our algorithm and the reference algorithm at one of the depths. Albeit having values that generally are higher than the reference, the trend of our $r_p(\theta_p)$ is still matching with the trend of the reference with a relatively small deviation. We can also see the effect of an unphysical dropouts on the inner radius estimation. In our inner radius curve, the unphysical dropout at the measurement around 170° is represented by a gap. On the other hand, the same unphysical dropout is represented by a downward spike on the reference curve. The different manifestation of unphysical dropouts on the inner radius values is due to the different way of handling dropouts in our algorithm and the reference algorithm. In our algorithm, the unphysical dropouts are replaced by a NaN value and ignored. The reference algorithm, on the other hand, seems to treat most of the unphysical dropouts as valid measurements. Thus, they are used to estimate the other inner geometry properties, resulting in significantly lower inner radius values on the measurement points at which the dropouts occur, as Figure 15 shows.

By calculating the average inner radii from every depth $\overline{r_p(\theta_p)}$, we can evaluate the overall accuracy of our estimated casing inner radius. Figure 16 shows a comparison between the average casing inner radius from algorithm and the reference, for every depth. It shows that our $\overline{r_p(\theta_p)}$ is generally slightly higher than that of the reference. The median of absolute deviation for our average inner radius is 0.0042 in, and the median of relative deviation is 0.099%. That implies that overall trend of our average inner radius is showing a good match with the reference with a relatively small deviation. Similar to the reference eccentering distance curve in Figure 13 and 14, the reference average casing inner radius in Figure 16 also shows multiple leftward spikes in the interval between XX92 m and XX01 m. As in the eccentering distance value, the spikes are caused by unphysical dropouts which are treated as a valid measurements by the reference algorithm (cf. Section 4.1). The unrealistic travel time values in these dropouts lead to unrealistic eccentering distance values, which in turn causes unrealistic reference inner radius values.

ISBN 978-82-8123-021-7

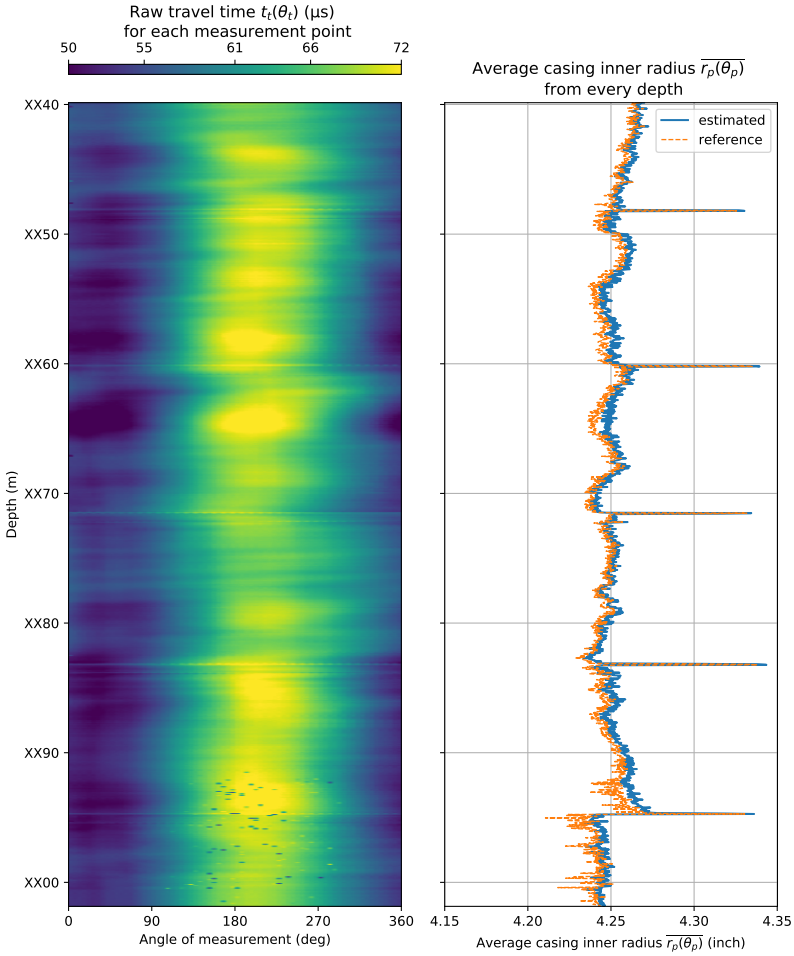

Figure 16: A comparison between the average casing inner radius $\overline{r_p(\theta_p)}$ from our algorithm and from the reference algorithm, for every depth. The spikes on the reference curve between XX92 m and XX01 m are caused by the unphysical dropouts shown in the travel time image plot.

The casing inner radius can also be displayed in an image plot, which is the common way of displaying ultrasonic cased hole logs. In the image plot, each pixel represents a measurement point. Figure 17 compares the casing inner radius estimated by our algorithm and the reference, throughout the entire log interval. It shows that the estimated inner radius has overall slightly higher values compared to the reference, as indicated by the color intensity of the estimated inner radius image plot. The deviation plot also displays a predominantly small and positive deviation[5], except on the measurement points at which dropouts are present. This implies that our estimated inner radius is generally slightly higher than the reference, similar to what is shown in Figure 16. This offset might be induced by a time offset or correction factor which is used to adjust the inner radius estimation in the reference algorithm [10]. Despite having an offset, the estimated inner radius image plot in general still has similar values and patterns with the reference. This indicates that our algorithm managed to produce casing inner radius with a good match to the reference, for most of the measurement points.

The reference inner radius image plot shown in Figure 17 displays plenty of distinctly colored pixels which occurs randomly between XX92 to XX01 m. In the reference algo-

[5]The deviation $\Delta r_p(\theta_p)$ is calculated as $\Delta r_p(\theta_p) = \text{estimated } r_p(\theta_p) - \text{reference } r_p(\theta_p)$.

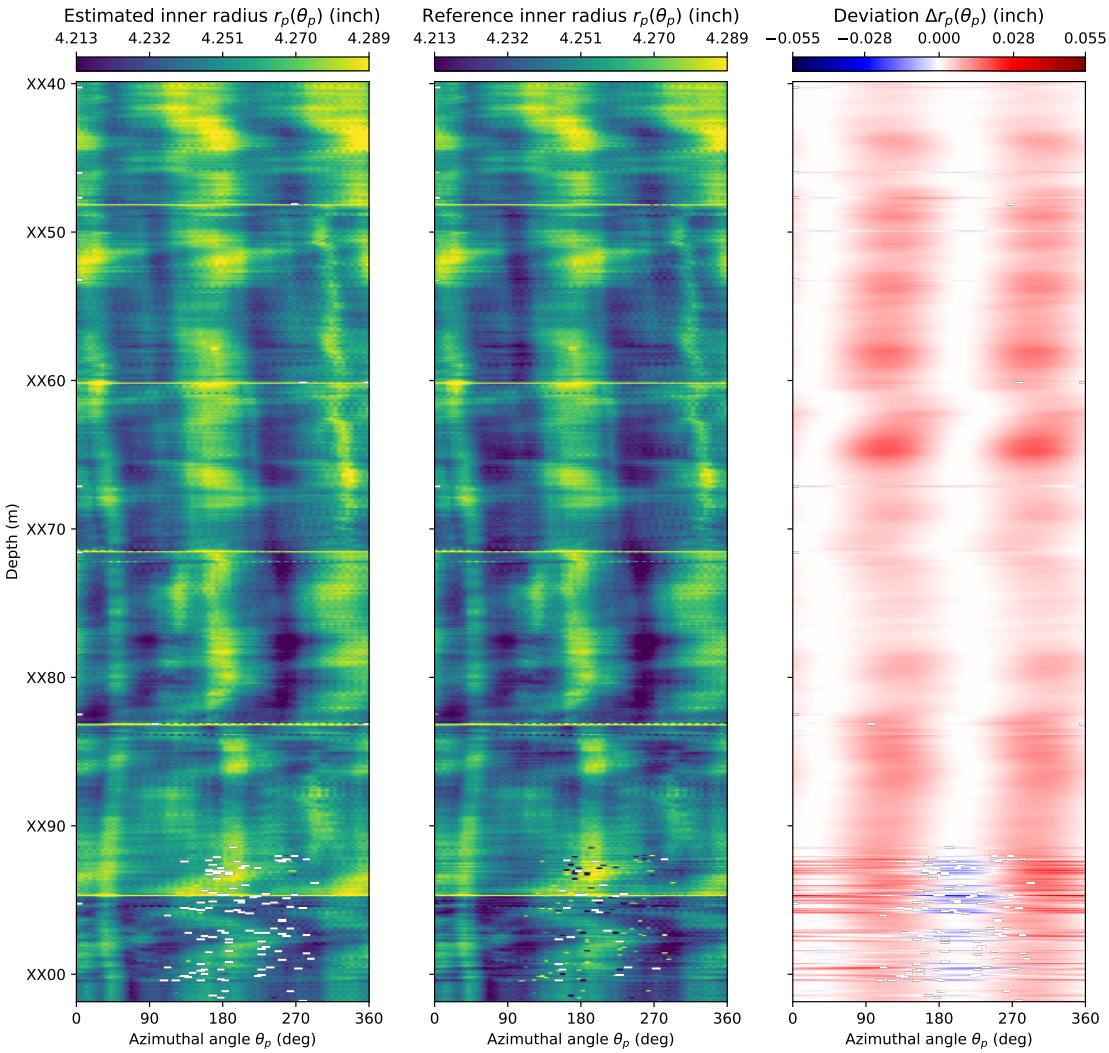

Figure 17: A comparison between the casing inner radius $r_p(\theta_p)$ from our algorithm and from the reference algorithm, for every measurement points in each depth. The difference between the estimated inner radius values with the reference is shown in the deviation plot.

rithm, most of these unphysical dropouts are treated as valid measurements which leads to unrealistic inner radius values displayed as the distinctly colored pixels. The effect of these dropouts is also visible in the deviation plot. We can see horizontal stripes in the interval between XX92 m and XX01 m, and on some depths above it, e.g. XX47 m or xx67 m. Those stripes are caused by dropouts leading to unrealistic eccentering distances which in turn are used to estimate the reference casing inner radius on those depths, resulting in unrealistic reference inner radius values at these depths. Hence, the deviations between the two algorithms are large at these depths, causing horizontal stripes that give a striking visual contrast with the surrounding area without dropouts.

5 Conclusion

In this study, we have successfully developed and tested a casing inner geometry determination algorithm. The algorithm is based on the ultrasonic pulse-echo technique and

ISBN 978-82-8123-021-7

trigonometric calculations to estimate the inner geometry properties of tool eccentering and casing inner radius.

The algorithm was developed with the aim of producing results which are similar to the results from the reference algorithm while also introducing improvements to the reference algorithm. Through the development of the algorithm, several key findings were observed:

- Electronic disturbances or signal processing errors during logging can result in unreliable travel time measurements in the well log data. Such unreliable measurements, i.e. poor travel time readings, can be significantly present in the well log. Since they do not represent any actual condition in the casing, they need to be handled properly.

- Eccentered measurements commonly occur during logging due to gravity or tool movement, and it affects the mechanism of the measurement and the distribution of measurement points on the inner perimeter of the casing. Hence, determining eccentering distance and angle is crucial for estimating the final product of the algorithm which is the casing inner radius.

- While the trigonometric principles of estimating eccentering properties seem relatively straightforward, the measured data seldom correspond to the ideal case that the trigonometric derivation assumes. Therefore, operations such as regression and optimization are necessary to estimate the eccentering properties.

- The casing inner radii that the algorithm estimates are not distributed evenly in azimuthal angle due to eccentered measurements. Although we have the option to induce an even sampling to the inner radius data through interpolation, it may alter the characteristics of the result, which may lead to a false impression of the actual condition of the casing. By keeping the uneven sampling of the casing inner radius data, we are actually preserving valuable information which might give insight on the actual condition of the casing.

The results of the developed algorithm were compared to the results of the reference algorithm from the service company. The comparison shows that our algorithm managed to produce very similar results. The eccentering properties estimated by our algorithm show a good match with the reference, with a median relative deviation of 0.0019% for the eccentering distance; and 0.0058% for the eccentering angle. The algorithm is also able to estimate casing inner radius values which show a similar pattern with the reference. The median of relative deviation for the casing inner radius is 0.099%, which implies that the inner radius estimated by the algorithm is having a relatively good match with the reference.

Besides being able to produce results with relatively low deviation from the reference, our algorithm also implements an improved way of handling faulty measurements which might have significant presence in the data. In our algorithm, the faulty travel time readings were handled by identifying and replacing them with empty values. This implies that the algorithm is able to produce a more reliable estimate of the inner geometry properties.

The algorithm described in this article can be implemented on a variety of well integrity log data, e.g. from the publicly available Volve Data Village dataset [9, 10]. By

ISBN 978-82-8123-021-7

implementing the algorithm on well log data from various different oil fields, several novel findings might be observed since the logging environment might be different from field to field. It is also possible to pursue further development in the algorithm, since it still has room for improvement. For example, the poor travel time readings can possibly be corrected based on the recorded waveforms, which could result in an even more reliable measurement. The algorithm can also be validated and improved even further by comparing it with a to a case with a ground truth, e.g. a precise lab measurement or simulated data. We hope that this article will enhance and spread the knowledge of ultrasonic cased hole logging, especially for those working in the processing of ultrasonic cased hole data or the development of ultrasonic cased hole logging tools.

6 Acknowledgements

The authors would like to thank Equinor for providing well log data and for their permission to publish this work. This work was supported by the Research Council of Norway under grant 237887.

References

[1] H. Devold, *Oil and Gas Production Handbook: An Introduction to Oil and Gas Production*. ABB Oil and Gas, 2013.

[2] J. Lecourtier, *Cementing Technology and Procedures*. Editions TECHNIP, 1993.

[3] A. A. Almukhaitah and S. Haldar, "Effective Well Integrity Management in a Mature Sour Oil Field," in *Proceedings of the International Petroleum Technology Conference*. OnePetro, 2013.

[4] A. J. Hayman, R. Hutin, and P. V. Wright, "High-Resolution Cementation And Corrosion Imaging By Ultrasound," in *Proceedings of the SPWLA 32nd Annual Logging Symposium*. OnePetro, Jun. 1991.

[5] E. B. Nelson and D. Guillot, *Well Cementing*. Schlumberger, 2006.

[6] M. Graham, "Correcting for eccentricity of acoustic sensors in wells and pipes," GB Patent GB2 585 328A, Jan., 2021. [Online]. Available: https://patents.google.com/patent/GB2585328A/en

[7] T. V. Zharnikov, M. Fukuhara, I. V. Borodin, and D. V. Pissarenko, "Method and a system for monitoring a logging tool position in a borehole," WO Patent WO2 010 019 070A1, Feb., 2010. [Online]. Available: https://patents.google.com/patent/WO2010019070A1/en

[8] W. Han and T. Wang, "Caliper Logging Using Circumferentially Spaced and/or Angled Transducer Elements," US Patent US20 100 154 531A1, Jun., 2010. [Online]. Available: https://patents.google.com/patent/US20100154531A1/en

[9] Equinor, "Volve Data Village dataset," 2018. [Online]. Available: https://data.equinor.com/

[10] E. M. Viggen, E. Hårstad, and J. Kvalsvik, "Getting started with acoustic well log data using the dlisio Python library on the Volve Data Village dataset," in *Proceedings of the 43rd Scandinavian Symposium on Physical Acoustics*, 2020, p. 36.

ISBN 978-82-8123-021-7